ARCHIVES OF MECHANICS
Arch. Mech. **78** (1), 3–31, 2026, https://doi.org/10.24423/aom.4808

An analytical model for ballistic performance prediction of elastoplastic materials with strain hardening

B. T. PHAN[1*], V. KULISH[2,3], V. HORÁK[1]

[1] *Department of Mechanical Engineering, Faculty of Military Technology, University of Defence, Brno, Czech Republic, e-mail*[*]*: buithanh.phan@unob.cz (corresponding author)*

[2] *Department of Computer Science & Department of Mathematics, Faculty of Science, University of South Bohemia, Česke Budějovice, Czech Republic*

[3] *Madanapalle Institute of Technology & Science, Deemed to be University, Madanapalle – 517325, Andhra Pradesh, India*

This study presents an analytical model to predict the ballistic performance of elastoplastic materials with strain hardening under normal impact by rigid penetrators. The model integrates the localized interaction model with the spherical cavity-expansion theory to account for dynamic material behaviour. Key parameters, including cavity-expansion pressure and strain hardening, are incorporated using the Ludwik and Voce hardening laws, enabling accurate predictions of residual velocity and ballistic limit. The model is validated using experimental data for various aluminium alloys and steel plates, demonstrating good agreement between predictions and observations. The proposed analytical approach offers a reliable and computationally efficient tool for evaluating ballistic performance, making it a valuable resource in armour design and impact mechanics research.

Key words: spherical cavity-expansion, localized interaction model, ballistic performance.

1. Introduction

The study of ballistic performance is critical for the design of protective materials in military, aerospace, and civil applications. Over the past few decades, significant efforts have been made to develop empirical, numerical, and analytical models to predict the response of materials under ballistic impact. While experimental research provides invaluable insights, it is often expensive and limited in scope. Numerical simulations, on the other hand, offer detailed results but are computationally intensive, especially for large-scale dynamic phenomena such as high-speed impacts. Consequently, there is a growing interest in analytical models that provide efficient and accurate predictions of ballistic performance.

For last few decades, many studies on ballistic performance of various materials have developed empirical or semi-empirical laws for the penetration through the analysis and induction of experimental data. While ballistic experimental research is quite expensive, and numerical simulations of such a high-speed dynamic phenomenon are often time-consuming for large-scale simulation despite recent advances in computational technology. The spherical cavity-expansion (SCE) theory has emerged as an attractive tool in analysing the penetration mechanics. Originally developed to describe the expansion of a cavity within an infinite medium under high-pressure conditions, the theory has evolved to incorporate complex material behaviours and dynamic effects, enhancing its relevance across a wide range of engineering applications. Specifically, analytical models based on the SCE theory have demonstrated accuracy and reliability on modelling ballistic impact response in various studies.

Early studies, such as the work of Hill [1], laid the groundwork by developing the quasi-static cavity-expansion theory. Building on this foundation, Forrestal and Luk [2] developed an analytical model for dynamic spherical cavity-expansion in elastic-perfectly plastic materials, which effectively predicted cavity-expansion over a practical range of cavity-expansion velocities. While Luk *et al.* [3] extended the theory to incorporate power-law strain hardening, providing closed-form analytical solutions for incompressible materials and numerical solutions for compressible materials.

Subsequent efforts aimed to integrate additional physical effects into the SCE model. Warren and Forrestal [4] introduced a penetration model based on the SCE theory that described the combined influences of compressibility, strain hardening, and strain-rate sensitivity. Fang *et al.* [5] developed a SCE model for Tresca and Mohr–Coulomb materials that account for free surface effects by introducing a decay function. Ga *et al.* [6] presented a spherical cavity-expansion model that considers dynamic hardening including plastic strain, plastic strain rate, and temperature for an infinite compressible medium.

SCE models have been extended to account for projectile geometries and mechanical properties of targets. For example, Forrestal and Warren [7] proposed penetration equations for rigid ogive-nose projectiles that penetrate aluminium targets. Liu *et al.* [8] developed a 3D analytical model for the oblique penetration of tungsten spheres against low-carbon steel targets based on the SCE theory and the resistance decay model. While Rosenberg and Dekel [9] provided analytical solutions for the dynamic spherical cavity-expansion in an elastoplastic solid obeying von-Mises yield criterion. Notably, an extensive search for material similarities was performed to highlight the roles of the elastic properties of the solid, as well as its strength and equation of state parameters. Durban and Masri [10] incorporated Drucker–Prager yield criteria, non-associated flow rules and arbitrary strain-hardening for pressure-sensitive solids,

providing a general theoretical basis for numerical evaluation of cavity-expansion pressure. Instead of extending the fundamental theoretical structure of their formulation, the present study reformulates the spherical cavity-expansion response into an explicit analytical pressure-velocity representation that can be directly coupled with projectile motion equations for ballistic penetration analysis. In particular, the proposed polynomial approximation of the cavity-expansion pressure enables closed-form expressions for residual velocity and ballistic limit, which are more suitable for engineering applications such as armour design.

Applications of the SCE theory have expanded beyond metal materials to include concrete and geological media. For instance, He *et al.* [11] suggested a dynamic spherical cavity-expansion for concrete targets regarding shear dilatancy and compressibility. Deng *et al.* [12] presented an improved dynamic cavity-expansion model that considers reinforcement effects in reinforced-concrete targets. Varnosfaderani *et al.* [13] developed a model based on the spherical cavity-expansion theory to predict the deceleration rate and final penetration depth of a rigid projectile probe into geological targets under the subsonic impact.

Despite recent advancements in the SCE theory, key challenges remain, particularly in capturing the effects of strain hardening and complex target responses under extreme loading. Most previous works have focused on cavity-expansion models for materials with power-law strain hardening, but not accounting for nonlinear strain-hardening laws, such as Ludwik and Voce laws, which are essential for accurate description of modern materials. The present study generalises the spherical cavity-expansion model to include Ludwik and Voce laws, which are more representative of elastoplastic behaviour under high strain rates. Particularly, its novelty lies in constructing a computationally efficient analytical framework and demonstrating its applicability to nonlinear hardening laws (e.g., Ludwik and Voce), rather than in redefining the general arbitrary hardening theory itself.

The present study aims to present an analytical model for predicting the impact response of elastoplastic materials with strain hardening under ballistic impact of rigid penetrators. The analytical formulation is based on the localized interaction model associated with a spherical cavity-expansion model. By integrating advanced strain-hardening laws, the analytical model can account for nonlinear material responses under dynamic impact. Although the penetration problem is inherently dynamic, the quasi-static solution is included as a reference framework to validate the model's material response and stress-strain relationships under simplified conditions. This ensures that the assumptions underlying the dynamic model are grounded in physical reality. Additionally, model validation is performed on various materials, including aluminium alloys and steels, demonstrating broad applicability in evaluating ballistic performance and designing advanced protective materials.

2. Cavity-expansion model

2.1. Mathematical formulation

Assumptions

Consider dynamic expansion of a spherical cavity (Fig. 1), the following assumptions are made:

- A spherically symmetric cavity is expanded at constant velocity from zero initial radius.
- There are three distinguish regions, i.e., plastic, elastic, and undeformed regions.
- There is no jump at the elastic-plastic interface, i.e., continuous solution. It means that at the elastic-plastic interface, the particle velocities in the plastic and elastic regions are equal and so are the stresses.

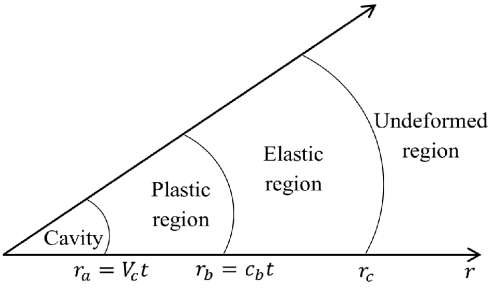

Fig. 1. Spherical cavity-expansion model.

Governing equations

In Eulerian spherical coordinates, the conservation of momentum and mass equations read:

$$\frac{\partial \sigma_r}{\partial r} + \frac{2(\sigma_r - \sigma_\theta)}{r} = -\rho\left(\frac{\partial v}{\partial t} + v\frac{\partial v}{\partial r}\right), \tag{2.1}$$

$$\rho\left(\frac{\partial v}{\partial r} + \frac{2v}{r}\right) = -\left(\frac{\partial \rho}{\partial t} + v\frac{\partial \rho}{\partial r}\right), \tag{2.2}$$

where v is the particle velocity measured positive outward, σ_r and σ_θ are radial and circumferential components of the Cauchy stress measured positive in compression.

In Eulerian spherical coordinates, the hydrostatic pressure p, the stress components σ_r and σ_θ satisfy the following relation

$$p = \frac{1}{3}(\sigma_r + 2\sigma_\theta). \tag{2.3}$$

Equation of state

A linear equation of state in this study is used to simplify the analytical framework, allowing for closed-form solutions and computational efficiency. While this approach is suitable for moderate velocity ranges, it does not capture the nonlinear pressure-strain behaviour observed in high-velocity penetration scenarios. Despite this limitation, the model demonstrates reasonable accuracy for the materials and velocities considered. Specifically, the material is characterized by a simple linear equation of state as follows:

$$p = K\left(1 - \frac{\rho_0}{\rho}\right) = K(\varepsilon_r + 2\varepsilon_\theta), \tag{2.4}$$

where p is the hydrostatic pressure, K is the bulk modulus, ε_r is the radial strain, ε_θ is the circumferential strain, ρ_0 and ρ are the densities in the undeformed and deformed configurations, respectively.

2.1.1. Elastic response

In the elastic region where strains are small, the radial strain ε_r and the circumferential strain ε_θ are expressed by:

$$\varepsilon_r = -\frac{\partial u}{\partial r}, \tag{2.5}$$

$$\varepsilon_\theta = -\frac{u}{r}, \tag{2.6}$$

where u is radial displacement measured positively outward.

For compressible materials, the radial and circumferential stresses according to Hooke's law are expressed by:

$$\sigma_r = -\frac{E}{(1+\nu)(1-2\nu)}\left[(1-\nu)\frac{\partial u}{\partial r} + 2\nu\frac{u}{r}\right], \tag{2.7}$$

$$\sigma_\theta = -\frac{E}{(1+\nu)(1-2\nu)}\left[\nu\frac{\partial u}{\partial r} + \frac{u}{r}\right], \tag{2.8}$$

where E is the elastic modulus and ν is Poisson's ratio.

For incompressible materials, the radial and circumferential stresses according to Hooke's law are expressed by the relations

$$\sigma_r - \sigma_\theta = E\varepsilon_r = -2E\varepsilon_\theta. \tag{2.9}$$

Plastic response

In the plastic region, the radial strain ε_r and circumferential strain ε_θ are given by:

$$\varepsilon_r = \ln\left(1 - \frac{\partial u}{\partial r}\right), \tag{2.10}$$

$$\varepsilon_\theta = \ln\left(1 - \frac{u}{r}\right). \tag{2.11}$$

Beyond the yielding point, the material is assumed to follow the strain hardening law

$$\sigma(\varepsilon_p) = Y + H(\varepsilon_p), \tag{2.12}$$

where σ is the true stress, ε_p is the plastic strain, Y is the initial yield stress, $H(\varepsilon_p)$ is the strain hardening function. In this study, two common strain hardening laws, namely Ludwik and Voce, are considered in the following forms, respectively:

$$\sigma(\varepsilon_p) = Y + B\varepsilon_p^n, \tag{2.13}$$

$$\sigma(\varepsilon_p) = Y + Q[1 - \exp(-C\varepsilon_p^n)]. \tag{2.14}$$

For spherical symmetry, the uniaxial radial stress state $(\sigma_r - \sigma_\theta, 0, 0)$ can be decomposed into the principal stress state $(\sigma_r, \sigma_\theta, \sigma_\theta)$ that produces radial strain ε_r and the isotropic stress state $(-\sigma_\theta, -\sigma_\theta, -\sigma_\theta)$ that produces radial strain $-\frac{(1-2\nu)}{E}\sigma_\theta$ [3]. Regarding the superposition principle, the uniaxial radial stress state $(\sigma_r - \sigma_\theta, 0, 0)$ produces the total strain ε as

$$\varepsilon = \varepsilon_r - \frac{(1-2\nu)}{E}\sigma_\theta, \tag{2.15}$$

and using Eqs. (2.3) and (2.4), the total strain ε can be also written in term of ε_θ as

$$\varepsilon = -2\varepsilon_\theta + \frac{(1-2\nu)}{E}(\sigma_r + \sigma_\theta). \tag{2.16}$$

Additionally, for large deformation of metals such as steels and aluminium alloys where elastic strain is much smaller than the plastic strain, the total plastic strain can be approximately expressed by the plastic strain as $\varepsilon \approx \varepsilon_p$.

For incompressible materials, i.e., $\nu = \frac{1}{2}$, regarding Eqs. (2.15) and (2.16) the total strain ε is

$$\varepsilon = \varepsilon_r = -2\varepsilon_\theta. \tag{2.17}$$

Based on Eq. (2.11) and conservation of mass, the circumferential strain ε_θ is given by

$$\varepsilon_\theta = \ln\left(1 - \frac{u}{r}\right) = \frac{1}{3}\ln\left[1 - \frac{r^3 - (r-u)^3}{r^3}\right] = \frac{1}{3}\ln\left(1 - \frac{r_a^3}{r^3}\right), \tag{2.18}$$

where r_a is the radius of the cavity. Subsequently, the plastic strain ε_p for incompressible materials can be written as

$$\varepsilon_p \approx -\frac{2}{3}\ln\left(1-\frac{r_a^3}{r^3}\right). \tag{2.19}$$

2.2. Quasi-static solution

The quasi-static solution discussed in this study is not intended to directly represent the dynamic penetration process. Instead, it provides a baseline for understanding material behaviour in the absence of dynamic effects such as strain-rate sensitivity and inertial contributions. By comparing the quasi-static and dynamic solutions, we can better isolate and analyse the impact of these dynamic factors on the overall penetration process. For a quasi-static solution when the cavity-expansion velocity is small, inertial terms can be neglected and the conservation of momentum equation Eq. (2.1) is simplified into the form:

$$\frac{\partial \sigma_r}{\partial r}+\frac{2(\sigma_r-\sigma_\theta)}{r}=0. \tag{2.20}$$

2.2.1. Elastic region

Substituting Eqs. (2.7) and (2.8) into Eq. (2.20) yields

$$\frac{\partial^2 u}{\partial r^2}+\frac{2}{r}\frac{\partial u}{\partial r}-\frac{2u}{r^2}=0. \tag{2.21}$$

The solution of Eq. (2.21) is given by

$$u=C_1 r+\frac{C_2}{r^2}, \tag{2.22}$$

where C_1 and C_2 are the constants of integration which can be determined by the boundary condition, i.e., the zero displacement at the elastic wave front $u|_{r=r_c}=0$ and yield criterion at the elastic-plastic interface $(\sigma_r-\sigma_\theta)|_{r=r_b}=Y$ as follows:

$$C_1=-\frac{C_2}{r_c^3}, \tag{2.23}$$

$$\frac{E}{(1+\nu)}\left(\frac{u}{r}-\frac{\partial u}{\partial r}\right)\bigg|_{r=r_b}=\frac{E}{(1+\nu)}\frac{3C_2}{r^3}\bigg|_{r=r_b}=Y. \tag{2.24}$$

Solving Eq. (2.24) yields

$$C_2=\frac{(1+\nu)Y}{3E}r_b^3. \tag{2.25}$$

For compressible materials, substituting Eq. (2.22) into Eqs. (2.7) and (2.8) the radial and circumferential stresses are expressed respectively by:

$$\sigma_r = \frac{E}{(1+\nu)(1-2\nu)}\left[(1-2\nu)\frac{2C_2}{r^3} + (1+\nu)\frac{C_2}{\delta^3}\right] = \left[2\frac{r_b^3}{r^3} + \frac{(1+\nu)}{(1-2\nu)}\,\frac{r_b^3}{r_c^3}\right]\frac{Y}{3}, \tag{2.26}$$

$$\sigma_\theta = \frac{E}{(1+\nu)(1-2\nu)}\left[-(1-2\nu)\frac{C_2}{r^3} + (1+\nu)\frac{C_2}{\delta^3}\right] = \left[-\frac{r_b^3}{r^3} + \frac{(1+\nu)}{(1-2\nu)}\,\frac{r_b^3}{r_c^3}\right]\frac{Y}{3}, \tag{2.27}$$

and thus, the radial stress $\sigma_r|_{r=r_b}$ on the elastic-plastic interface is expressed by

$$\sigma_r|_{r=r_b} = \left[2 + \frac{(1+\nu)}{(1-2\nu)}\,\frac{r_b^3}{r_c^3}\right]\frac{Y}{3} \approx \frac{2}{3}Y. \tag{2.28}$$

Plastic region

For incompressible materials, it is more feasible to derive the solutions analytically. Specifically, substituting $\sigma_r - \sigma_\theta = Y + H(\varepsilon_p)$ into Eq. (2.20) yields

$$\frac{\partial \sigma_r}{\partial r} + 2\frac{Y + H(\varepsilon_p)}{r} = 0, \tag{2.29}$$

and considering the radial stress $\sigma_r|_{r=r_b} \approx \frac{2}{3}Y$ on the elastic-plastic interface given by Eq. (2.28), integrating Eq. (2.29) gives the solution σ_r as

$$\sigma_r \approx \frac{2}{3}Y - 2Y\ln\frac{r}{r_b} - 2\int_{r_b}^{r}\frac{H(\varepsilon_p)}{r}\,dr. \tag{2.30}$$

Subsequently, the radial stress $\sigma_r|_{r=r_a}$ on the cavity surface is

$$\sigma_r|_{r=r_a} \approx \frac{2}{3}Y - 2Y\ln\frac{r_a}{r_b} - 2\int_{r_b}^{r_a}\frac{H(\varepsilon_p)}{r}\,dr. \tag{2.31}$$

The conservation of mass equation, Eq. (2.2), for incompressible materials is simplified as follows:

$$\frac{\partial v}{\partial r} + \frac{2v}{r} = 0, \tag{2.32}$$

and considering the velocity $v|_{r=r_b} = \frac{\partial u}{\partial t}\big|_{r=r_b} = \frac{3Y}{2E}\frac{r_b^2}{r^2}\frac{\partial r_b}{\partial t}\big|_{r=r_b} = \frac{3Y}{2E}r_b^2 c_b$ on the elastic-plastic interface which is derived from Eq. (2.22), integrating Eq. (2.32) gives the solution v as

$$v = \frac{3Y}{2E}\frac{r_b^2}{r^2}c_b. \tag{2.33}$$

Subsequently, the velocity $v|_{r=r_a} = V_c$ on the cavity surface is

$$V_c = \frac{3Y}{2E}\frac{r_b^2}{r_a^2}c_b, \tag{2.34}$$

and note that $\frac{r_a}{r_b} = \frac{V_c}{c_b}$, Eq. (2.34) is simplified as

$$\frac{r_a}{r_b} = \left(\frac{3Y}{2E}\right)^{1/3}. \tag{2.35}$$

Substituting Eq. (2.35) into Eq. (2.31), the radial stress $\sigma_s = \sigma_r|_{r=r_a}$ on the cavity surface is

$$\sigma_s = \sigma_r|_{r=r_a} \approx \frac{2Y}{3}\left(1 + \ln\frac{2E}{3Y}\right) + I, \tag{2.36}$$

where the integral $I = 2\int_{r_a}^{r_b}\frac{H(\varepsilon_p)}{r}dr$ is determined based on the strain hardening law.

For the Ludwik law, the integral I is simplified by $x = \frac{r_a^3}{r^3}$ and $\frac{r_a}{r_b} = \left(\frac{3Y}{2E}\right)^{1/3}$ as

$$I = 2\int_{r_a}^{r_b}\frac{B\left[-\frac{2}{3}\ln\left(1-\frac{r_a^3}{r^3}\right)\right]^n}{r}dr = \left(\frac{2}{3}\right)^{n+1}B\int_{\frac{3Y}{2E}}^{1}\frac{[-\ln(1-x)]^n}{x}dx. \tag{2.37}$$

For the Voce law, the integral I is simplified by $x = \frac{r_a^3}{r^3}$ and $\frac{r_a}{r_b} = (\frac{3Y}{2E})^{1/3}$ as

$$\begin{aligned} I &= 2\int_{r_a}^{r_b}\frac{Q\left\{1-\exp\left[\frac{2C}{3}\ln\left(1-\frac{r_a^3}{r^3}\right)\right]\right\}}{r}dr \\ &= \frac{2Q}{3}\left[\ln\frac{2E}{3Y} - \int_{\frac{3Y}{2E}}^{1}\frac{(1-x)^{\frac{2C}{3}}}{x}dx\right]. \end{aligned} \tag{2.38}$$

By extending the results for the N-term Ludwik law $\sigma = Y + \sum_{i=1}^{N}B_i\varepsilon_p^{n_i}$, the N-term Voce law $\sigma = Y + \sum_{i=1}^{N}Q_i[1-\exp(-C_i\varepsilon_p^{n_i})]$ and their combined

law, the integral I can be expressed as $I = \sum_i^N I_i$, where the integral term I_i is computed according to the strain hardening law used.

For compressible materials, solving the governing equations analytically is more complicated due to the complexity of these equations. Hill [1] suggested an analytical expression for radial stress on the cavity surface for perfectly plastic compressible materials as

$$\sigma_s = \frac{2Y}{3}\left[1 + \ln\frac{E}{3(1-\nu)Y}\right]. \tag{2.39}$$

In the present study, radial stress on the cavity surface for compressible materials with strain hardening is supposed to take the form:

$$\sigma_s = \frac{2Y}{3}\left[1 + \ln\frac{E}{3(1-\nu)Y}\right] + I. \tag{2.40}$$

2.3. Cavity-expansion pressure

According to the study [4], the radial stress on the cavity surface, i.e., the cavity-expansion pressure, can be accurately approximated with a second-order polynomial of the cavity-expansion velocity V_c in the form:

$$\sigma_c = A_0 Y + A_1\sqrt{\rho_0 Y}V_c + A_2\rho_0 V_c^2, \tag{2.41}$$

where A_0, A_1, and A_2 are the dimensionless coefficients. In general, these coefficients can be determined via data regression by fitting Eq. (2.41) to the numerical solution of the cavity-expansion pressure, which is obtained by solving the governing spherical cavity-expansion equations. Besides, they can also be derived from an analytical approach as follows.

The first coefficient A_0 corresponds to the quasi-static cavity-expansion pressure and can be analytically derived from the quasi-static solution Eq. (2.40) in the previous section as

$$A_0 = \frac{2}{3}\left[1 + \ln\frac{E}{3(1-\nu)Y}\right] + \frac{I}{Y}. \tag{2.42}$$

The other coefficients A_1 and A_2 characterize the nonlinear relationship between the cavity-expansion pressure σ_c and the cavity-expansion velocity V_c. The terms $A_1\sqrt{\rho_0 Y}V_c$ and $A_2\rho_0 V_c^2$ arise from the high-velocity regime, where the material response becomes strongly nonlinear due to effects such as material compressibility, strain rate sensitivity, and visco-plasticity. Specifically, at high impact velocities where compressibility effects dominate, the coefficients A_1 and A_2 can be inversely proportional to the material bulk modulus K, i.e., A_1 and $A_2 \propto \frac{1}{K}$. If the stress-strain relationship is strain-rate sensitive, these coefficients can be

scaled with strain-rate sensitivity parameters in constitutive models such as the Johnson–Cook or Cowper–Symonds model. These coefficients can include friction or energy dissipation mechanisms. In addition, the term $A_2\rho_0 V_c^2$ may also represent viscous drag-like effects, analogous to fluid resistance.

On dynamic spherical cavity-expansions, WALKER [14] derived the cavity-expansion pressure for perfectly plastic compressible materials as follows:

$$\sigma_c = \frac{2Y}{3}\left[1 + \ln\frac{E}{3(1-\nu)Y}\right] + \rho_0 V_c^2. \tag{2.43}$$

In the present study, the cavity-expansion pressure for compressible materials with strain hardening is introduced to take the form:

$$\sigma_c = \frac{2Y}{3}\left[1 + \ln\frac{E}{3(1-\nu)Y}\right] + I + \rho_0 V_c^2, \tag{2.44}$$

where I takes into account the strain hardening effect and is determined based on the strain hardening law as mentioned in the previous section.

While analytical derivation of the coefficients A_0, A_1, and A_2 is challenging or involves many assumptions, it is more likely to determine them empirically via data regression. Specifically, these coefficients appear in the relationship between impact velocity and residual velocity (see Section 3.3).

2.4. Numerical solution

Introducing similarity transformations $\xi = \frac{r}{c_b t}$ and $\bar{u} = \frac{u}{c_b t}$ suggested by FORRESTAL and LUK [2], and dimensionless variables $S_r = \frac{\sigma_r}{K}$, $S_\theta = \frac{\sigma_\theta}{K}$, $T = S_r - S_\theta$, $U = \frac{v}{c_b}$, the conservation of momentum equation (2.1), the conservation of mass equation (2.2), and the equation of state (2.4) transform to the forms:

$$\frac{dS_r}{d\xi} + \frac{2}{\xi}T = \frac{c_b^2\rho}{K}(\xi - U)\frac{dU}{d\xi}, \tag{2.45}$$

$$\frac{dU}{d\xi} + \frac{2U}{\xi} = \frac{1}{\rho}(\xi - U)\frac{d\rho}{d\xi}, \tag{2.46}$$

$$1 - \frac{\rho_0}{\rho} = S_r - \frac{2}{3}T. \tag{2.47}$$

Differentiating Eq. (2.47) with respect to ξ yields the differential form:

$$\frac{\rho_0}{\rho^2}\frac{d\rho}{d\xi} = \frac{dS_r}{d\xi} - \frac{2}{3}\frac{dT}{d\xi}. \tag{2.48}$$

Note that the dimensionless particle velocity U relates to the dimensionless displacement $\bar{u}$ by

$$U = \frac{v}{c_b} = \frac{1}{c_b}\frac{\partial u}{\partial t} = \frac{\partial(t\bar{u})}{\partial t} = \bar{u} + t\frac{\partial \bar{u}}{\partial t} = \bar{u} + t\frac{\partial \xi}{\partial t}\frac{\partial \bar{u}}{\partial \xi} = \bar{u} - \xi\frac{d\bar{u}}{d\xi}, \tag{2.49}$$

and thus, the derivative $\frac{d\bar{u}}{d\xi}$ is written as

$$\frac{d\bar{u}}{d\xi} = \frac{\bar{u} - U}{\xi}. \tag{2.50}$$

In the elastic region, adopting the similarity transformations, the radial stress, Eq. (2.7), and the circumferential stress, Eq. (2.8), are transformed to the dimensionless radial stress S_r and the dimensionless circumferential stress S_θ, respectively, as:

$$S_r = -\frac{3}{(1+\nu)}\left[(1-\nu)\frac{d\bar{u}}{d\xi} + 2\nu\frac{\bar{u}}{\xi}\right], \tag{2.51}$$

$$S_\theta = -\frac{3}{(1+\nu)}\left[\nu\frac{d\bar{u}}{d\xi} + \frac{\bar{u}}{\xi}\right]. \tag{2.52}$$

Subsequently, the dimensionless stress $T = S_r - S_\theta$ and its derivative with respect to ξ are given respectively by:

$$T = \frac{3(1-2\nu)}{(1+\nu)}\left(\frac{\bar{u}}{\xi} - \frac{d\bar{u}}{d\xi}\right) = \frac{3(1-2\nu)}{(1+\nu)}\,\frac{U}{\xi}, \tag{2.53}$$

$$\frac{dT}{d\xi} = \frac{3(1-2\nu)}{(1+\nu)}\left(\frac{1}{\xi}\frac{dU}{d\xi} - \frac{U}{\xi^2}\right). \tag{2.54}$$

In the plastic region, adopting the similarity transformations, the radial strain and the circumferential strain are expressed as $\varepsilon_r = \ln\big(1 - \frac{\partial u}{\partial r}\big) = \ln\big(1 - \frac{d\bar{u}}{d\xi}\big)$ and $\varepsilon_\theta = \ln\big(1 - \frac{u}{r}\big) = \ln\big(1 - \frac{\bar{u}}{\xi}\big)$, respectively. Subsequently, the total strain Eq. (2.15) and its derivative with respect to ξ are expressed by:

$$\varepsilon = \ln\left(1 - \frac{d\bar{u}}{d\xi}\right) - \frac{S_r}{3} + \frac{T}{3}, \tag{2.55}$$

$$\frac{d\varepsilon}{d\xi} = \frac{1}{\xi\big(1 - \frac{d\bar{u}}{d\xi}\big)}\frac{dU}{d\xi} - \frac{1}{3}\frac{dS_r}{d\xi} + \frac{1}{3}\frac{dT}{d\xi}. \tag{2.56}$$

Beyond the yielding point, the material follows the strain hardening law, which is expressed in the dimensionless form and in its differential form as:

$$T = S_r - S_\theta = \frac{Y + H(\varepsilon)}{K}, \tag{2.57}$$

$$\frac{dT}{d\xi} = \frac{1}{K}\frac{dH(\varepsilon)}{d\varepsilon}\frac{d\varepsilon}{d\xi} = \frac{1}{K}\frac{dH(\varepsilon)}{d\varepsilon}. \tag{2.58}$$

The numerical solution can be obtained by directly solving the transformed governing equations of the spherical cavity-expansion model, namely the conservation of momentum equation (2.45), the conservation of mass equation (2.46), together with the equation of state (2.47), the constitutive relations (2.51) and (2.52) as well as the adopted strain-hardening law Eq. (2.57). The elastic

and plastic regions were treated separately, and continuity conditions at the elastic-plastic interface were enforced to ensure a consistent solution. The system of ordinary differential equations (2.45), (2.46), (2.48), (2.50), (2.54) for the elastic region and the system of ordinary differential equations (2.45), (2.46), (2.48), (2.50), (2.58) for the plastic region with the continuity conditions at the elastic-plastic interface $\bar{u}|_{\xi=1^+} = \bar{u}|_{\xi=1^-}$, $U|_{\xi=1^+} = U|_{\xi=1^-}$, $S_r|_{\xi=1^+} = S_r|_{\xi=1^-}$, $T|_{\xi=1^+} = T|_{\xi=1^-}$, $\rho|_{\xi=1^+} = \rho|_{\xi=1^-}$, are solved by numerical integration using the fourth order Runge–Kutta method implemented on MATLAB. As a result, the cavity-expansion pressure σ_c is extracted as the radial stress $\sigma_r|_{r=r_a} = KS_r|_{\xi=V_c/c_b}$ at the cavity surface.

3. Penetration model

3.1. Mathematical formulation

The localized interaction model, widely employed in penetration mechanics, assumes that interaction between a penetrator and a target can be represented as a superposition of the independent local interactions at the penetrator–target interface. Under this framework, the interaction between the penetrator and the target can be mathematically described in the general form:

$$d\boldsymbol{F} = (\sigma_n \hat{\boldsymbol{n}} + \sigma_\tau \hat{\boldsymbol{\tau}}) dS, \tag{3.1}$$

$$\hat{\boldsymbol{\tau}} = -\frac{\hat{\boldsymbol{v}} + \cos\theta \hat{\boldsymbol{n}}}{\sin\theta}, \tag{3.2}$$

$$\cos\theta = -\hat{\boldsymbol{v}} \cdot \hat{\boldsymbol{n}}, \tag{3.3}$$

where $d\boldsymbol{F}$ denotes the force acting on the surface element dS of the penetrator that is in contact with the target; $\hat{\boldsymbol{v}}$ is the unit vector of the velocity $\boldsymbol{V}$ of the surface element dS; $\hat{\boldsymbol{n}}$ and $\hat{\boldsymbol{\tau}}$ are the unit inward normal vector and the unit tangent vector to the surface element dS, respectively; and θ is the angle between the vector $\hat{\boldsymbol{n}}$ and the vector $-\hat{\boldsymbol{v}}$. Non-negative functions σ_n and σ_τ are the normal and tangential stresses on the surface element dS, respectively (see Fig. 2) [15, 16].

The normal stress σ_n acting on the surface element dS is supposed to be a function of the normal component V_n of the velocity $\boldsymbol{V}$ as follows:

$$\sigma_n = \sigma_n(V_n) = a_0 + a_1 V_n + a_2 V_n^2, \tag{3.4}$$

$$V_n = \boldsymbol{V} \cdot (-\hat{\boldsymbol{n}}) = V\hat{\boldsymbol{v}} \cdot (-\hat{\boldsymbol{n}}) = V\cos\theta, \tag{3.5}$$

where a_0, a_1 and a_2 are material-dependent parameters that characterize the target resistance. Specifically, the first term a_0 represents the quasi-static pressure associated with the elasticplastic deformation of the target, while the other

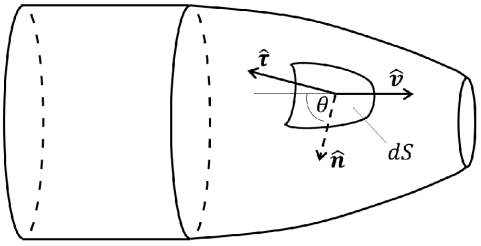

Fig. 2. Outline of localized interaction model [16].

terms a_1 and a_2 account for the dynamic pressure related to the dynamic response of the target.

The tangential stress σ_τ acting on the contact surface represents the friction between the penetrator and the target. The tangential stress σ_τ is commonly assumed to be proportional to the normal stress σ_n by the relation

$$\sigma_\tau = \mu\sigma_n, \tag{3.6}$$

in which μ is the friction coefficient at the penetrator–target interface.

In this approach, each infinitesimal element of the penetrator surface interacts locally with the surrounding target material, and the overall target resistance experienced by the penetrator is obtained by integrating local contributions over the contact surface. As a result, the total resistive force $\boldsymbol{F}$ exerted on the penetrator is expressed by the surface integral with respect to the infinitesimal resistive force $d\boldsymbol{F}$ over the contact surface S as

$$\mathbf{F} = \iint\limits_S d\,\mathbf{F} = \iint\limits_S [\sigma_n(\theta, v)\hat{\boldsymbol{n}} + \sigma_\tau(\theta, v)\hat{\boldsymbol{\tau}}]\, dS. \tag{3.7}$$

Consider the normal impact of an axisymmetric rigid penetrator with a diameter $d = 2R$ on a finite-thickness target, the total resistive force $\boldsymbol{F}$ can be represented in scalar form F along the penetration direction as a function of penetrator velocity V as

$$F = \pi R^2(N_0 a_0 + N_1 a_1 V + N_2 a_2 V^2), \tag{3.8}$$

where N_0, N_1 and N_2 are dimensionless shape factors that characterize the influence of the penetrator nose geometry on the target resistance. These factors arise from the integration of local interaction stresses over the penetrator nose surface. In case of frictionless contact, i.e., $\mu = 0$, the shape factors for common penetrator geometries are summarized in Table 1.

Table 1. Shape factors without considering friction [16, 17].

Nose shape	N_0	N_1	N_2
Flat	1	1	1
Hemispherical	1	$\frac{2}{3}$	$\frac{1}{2}$
Ogive	1	$\frac{1}{3}+\frac{1}{6\psi}$	$\frac{1}{3\psi}-\frac{1}{24\psi^2}$
Conical	1	$\sin\phi$	$\sin^2\phi$
Truncated conical	1	$\left[1-(\frac{d_0}{d})^2\right]\sin\phi$	$\left[1-(\frac{d_0}{d})^2\right]\sin^2\phi$

Note: $\psi = R_O/d$ is the calibre head radius (CRH), R_O is the ogive radius, ϕ is the semi-angle of cone and d_0 is the meplat diameter.

According to Newton's second law, the equation of motion of the penetrator is written in a time-independent form as

$$\varphi M V \frac{dV}{dz} = -F(z), \tag{3.9}$$

where M is the mass of the penetrator, V is the velocity of the penetrator and z is the travel distance of the penetrator, i.e., the instantaneous depth of penetration. The parameter φ represents a scaling factor that accounts for deviations between the idealised spherical cavity-expansion assumption and the actual localised projectile-target contact configuration. While the SCE model describes symmetric radial expansion in a semi-infinite medium, real penetration involves a finite-thickness target, localized plastic flow, and non-uniform stress distribution in the interaction zone. The factor φ therefore scales the effective target resistance acting on the projectile without modifying the governing form of Newton's second law. It should not be interpreted as an arbitrary empirical constant, but rather as a geometry-dependent interaction parameter associated with a given projectile–material pair. In the present study, φ is determined by a least-squares regression to ballistic experimental data. Once calibrated, φ remains constant for a given projectile–target contact configuration, allowing the model to predict the residual velocity of the projectile and the ballistic limit of the target.

Note that the normal stress σ_n on the penetrator surface is equal to the cavity-expansion pressure σ_c and velocity component V_n normal to the penetrator surface is equal to cavity-expansion velocity V_c. Equating Eqs. (2.41) and (3.4) yield the parameters $a_0 = A_0 Y$, $a_1 = A_1\sqrt{\rho_0 Y}$ and $a_2 = A_2\rho_0$. Hence, the resistive force F is expressed by

$$F = \pi R^2(N_0 A_0 Y + N_1 A_1\sqrt{\rho_0 Y}V + N_2 A_2\rho_0 V^2). \tag{3.10}$$

Substituting Eq. (3.10) into Eq. (3.9) and rearranging, the equation of motion of the penetrator simplifies to

$$V\frac{dV}{dz} = -(\alpha + \beta V + \gamma V^2), \tag{3.11}$$

where $\alpha = \frac{\pi R^2}{\varphi M} N_0 A_0 Y$, $\beta = \frac{\pi R^2}{\varphi M} N_1 A_1 \sqrt{\rho_0 Y}$ and $\gamma = \frac{\pi R^2}{\varphi M} N_2 A_2 \rho_0$.

3.2. Physical constraints on model parameters

As the penetrator penetrates the target, the resistive force F grows with V^2, reflecting nonlinear energy dissipation mechanisms like plastic deformation and strain hardening. It implies the penetrator's velocity decreases monotonically during the process of penetration. For monotonic decay of penetrator's velocity, it requires some specific constraints applied on the governing differential equation (3.11) and thus on the model parameters α, β, and γ as follows:

a) $\gamma \geq 0$;
b) if $\gamma = 0$ then $\alpha > 0$ and $\beta > 0$;
c) if $\gamma > 0$ then either $\Delta = \beta^2 - 4\gamma\alpha < 0$ or $\Delta = \beta^2 - 4\gamma\alpha \geq 0$, $\alpha > 0$ and $\beta < 0$.
(The quadratic $\alpha+\beta V+\gamma V^2$ has either complex roots or positive real roots.)

3.3. Solution

Rearranging for separation of variables and integrating Eq. (3.11) yields

$$\int \frac{V\,dV}{\alpha + \beta V + \gamma V^2} = -\int dz. \tag{3.12}$$

Consider the mentioned physical constraints in the previous section, three scenarios are analysed as follows:

Case 1: $\alpha > 0$, $\beta > 0$ and $\gamma = 0$

Considering the initial condition $V|_{z=0} = V_0$ and evaluating the integrals in Eq. (3.12), the velocity V is implicitly expressed by

$$V_0 - V - \frac{\alpha}{\beta}\ln\left(\frac{\alpha + \beta V_0}{\alpha + \beta \mathrm{V}}\right) = \beta z. \tag{3.13}$$

The ballistic limit V_b for the target of the thickness h is implicitly expressed by substitutions $z = h$, $V_0 = V_b$ and $V = 0$ into Eq. (3.13) as

$$V_b - \frac{\alpha}{\beta}\ln\left(\frac{\alpha + \beta V_b}{\alpha}\right) = \beta h. \tag{3.14}$$

Case 2: $\Delta = \beta^2 - 4\gamma\alpha \geq 0$, $\alpha > 0$, $\beta < 0$ and $\gamma > 0$

The quadratic $\alpha + \beta V + \gamma V^2$ has real roots $V_1 = \frac{-\beta+\sqrt{\Delta}}{2\gamma}$ and $V_2 = \frac{-\beta-\sqrt{\Delta}}{2\gamma}$. Using partial fraction decomposition, Eq. (3.12) is rewritten as

$$\frac{1}{\beta}\int\left(\frac{V_2}{V-V_1}+\frac{V_1}{V-V_2}\right)dV = \int dz. \tag{3.15}$$

Considering the initial condition $V|_{z=0} = V_0$ and evaluating the integrals, the velocity V is implicitly expressed by

$$V_2\ln\left(\frac{V-V_1}{V_0-V_1}\right)+V_1\ln\left(\frac{V-V_2}{V_0-V_2}\right) = \beta z. \tag{3.16}$$

The ballistic limit V_b for the target of the thickness h is implicitly expressed by substitutions $z = h$, $V_0 = V_b$ and $V = 0$ into Eq. (3.16) as

$$V_2\ln\left(\frac{-V_1}{V_b-V_1}\right)+V_1\ln\left(\frac{-V_2}{V_b-V_2}\right) = \beta h. \tag{3.17}$$

If $V_1 = V_2 = -\frac{\beta}{2\gamma}$, then the velocity V is explicitly expressed by

$$V = V_1 + (V_0 - V_1)\exp(2V_1\beta z) = -\frac{\beta}{2\gamma}+\left(V_0+\frac{\beta}{2\gamma}\right)\exp\left(-\frac{\beta^2}{\gamma}z\right), \tag{3.18}$$

and the ballistic limit V_b is explicitly expressed by

$$V_b = V_1\left[1-\exp(-2V_1\beta h)\right] = -\frac{\beta}{2\gamma}\left[1-\exp\left(\frac{\beta^2}{\gamma}h\right)\right]. \tag{3.19}$$

Case 3: $\Delta = \beta^2 - 4\gamma\alpha < 0$, $\alpha > 0$ and $\gamma > 0$

Note that Eq. (3.11) belongs to Chini's equations. In this case $\Delta < 0$, the velocity V is implicitly expressed by

$$\ln\left(\frac{\alpha+\beta V+\gamma V^2}{\alpha+\beta V_0+\gamma V_0^2}\right) = \frac{2\beta\left[\tan^{-1}\left(\frac{\beta+2\gamma V}{\sqrt{4\gamma\alpha-\beta^2}}\right)-\tan^{-1}\left(\frac{\beta+2\gamma V_0}{\sqrt{4\gamma\alpha-\beta^2}}\right)\right]}{\sqrt{4\gamma\alpha-\beta^2}} - 2\gamma z. \tag{3.20}$$

The ballistic limit V_b for the target of the thickness h is implicitly expressed by substitutions $z = h$, $V_0 = V_b$ and $V = 0$ into Eq. (3.20) as

$$\ln\left(\frac{\alpha}{\alpha+\beta V_b+\gamma V_b^2}\right) = \frac{2\beta\left[\tan^{-1}\left(\frac{\beta}{\sqrt{4\gamma\alpha-\beta^2}}\right)-\tan^{-1}\left(\frac{\beta+2\gamma V_b}{\sqrt{4\gamma\alpha-\beta^2}}\right)\right]}{\sqrt{4\gamma\alpha-\beta^2}} - 2\gamma h. \tag{3.21}$$

Adopting the spherical cavity-expansion model proposed in Eq. (2.44), it implies that the model parameters $\alpha > 0$, $\beta = 0$, $\gamma > 0$ and thus $\Delta = \beta^2 - 4\gamma\alpha < 0$, i.e., case 3. Hence, the velocity V could be explicitly expressed by substitution $\beta = 0$ into Eq. (3.20) as

$$V = \sqrt{\left(\frac{\alpha}{\gamma} + V_0^2\right)\exp(-2\gamma z) - \frac{\alpha}{\gamma}}, \tag{3.22}$$

and subsequently, the ballistic limit V_b is explicitly expressed by substitutions $z = h$, $V_0 = V_b$ and $V = 0$ into Eq. (3.22) as

$$V_b = \sqrt{\frac{\alpha}{\gamma}[\exp(2\gamma h) - 1]}. \tag{3.23}$$

4. Model validation

The present model is validated by experimental data obtained from studies on ballistic performance of various aluminium alloys and steels. Material parameters for these metals are listed in Tables 2 and 3. The Ludwik and Voce hardening law are used in the calculations and comparisons presented in this section. This choice is made based on its suitability for representing the elasto-plastic behaviour of the materials studied.

Table 2. Material parameters for Ludwik hardening law for four aluminium alloys and steels.

Materials	Parameters					
	Density ρ [kg/m^3]	Elastic modulus E [GPa]	Poisson ratio ν [–]	Ludwik model		
				Y [MPa]	B [MPa]	n [–]
AA 7075-T651 [18]	2700	64	0.3	448.4	475.8	0.39
AA 5083-H116 [19]	2700	70	0.3	124	456	0.252
Weldox 460E [20]	7850	200	0.33	490	807	0.73
Weldox 700E [21]	7850	210	0.33	859	329	0.579

Table 3. Material parameters for Voce hardening law for four aluminium alloys and steels.

Materials	Parameters							
	Density ρ [kg/m^3]	Elastic modulus E [GPa]	Poisson ratio ν [–]	Voce model				
				Y [MPa]	Q_1 [MPa]	C_1 [–]	Q_1 [MPa]	C_1 [–]
AA6070-T6 [22]	2700	70	0.3	350.0	30.1	185.9	72.8	7.7
AA6082-T6 [23]	2700	70	0.3	307.3	4.3	278.7	97.1	14.1
Weldox 500E [24, 25]	7850	210	0.33	567.8	172.9	23.69	1356.0	0.22
Weldox 700E [24, 25]	7850	210	0.33	738.2	151.3	29.96	1980.0	0.13

4.1. Cavity-expansion model

To validate the analytical approximation of the cavity-expansion pressure, both analytical and numerical solutions are presented. The analytical solution used for comparison corresponds to Eq. (2.44), which represents the polynomial approximation of the cavity-expansion pressure as a function of cavity-expansion velocity. While the numerical solution is obtained from the numerical integration of the governing differential equations of the SCE model, which are described in Section 2.4, and the cavity-expansion pressure is calculated as the radial stress at the cavity surface. Figures 3–6 illustrate the analytical prediction from Eq. (2.44) and the numerical results of the cavity-expansion pressure σ_c for various aluminium alloys and steels. Good agreement between the numerical and analytical solutions was obtained.

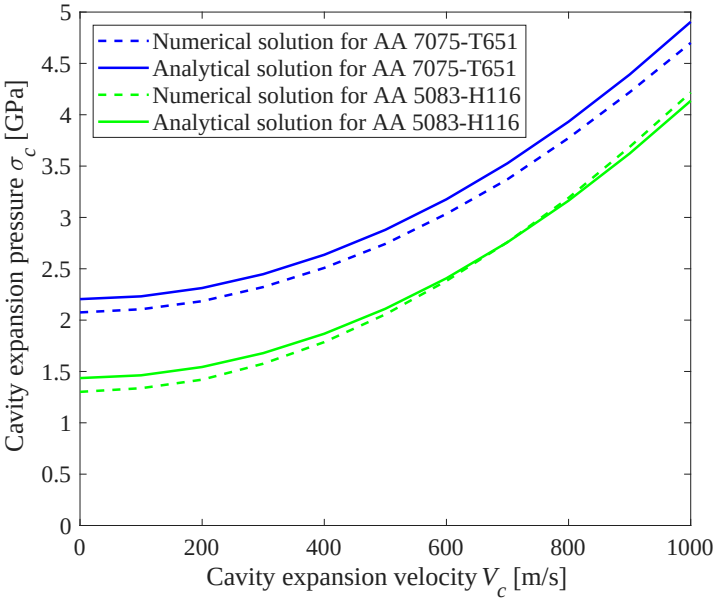

Fig. 3. Numerical and analytical solutions for cavity-expansion pressures as a function of cavity-expansion velocity for aluminium alloys AA 7075-T651 [18] and AA 5083-H116 [19]. Analytical solutions are obtained using Eq. (2.44).

Additionally, a least-squares regression procedure was employed to determine the coefficients A_0, A_1, and A_2 by fitting the polynomial representation Eq. (2.41) of the cavity-expansion pressure to the numerical solution of the cavity-expansion pressure obtained in the validation examples above. Through regression, it was noted that A_1 could be neglected, i.e., $A_1 = 0$, due to its relatively small value and negligible contribution to the cavity-expansion pressure. The fitted values of the coefficients A_0 and A_2 along with their analytical values,

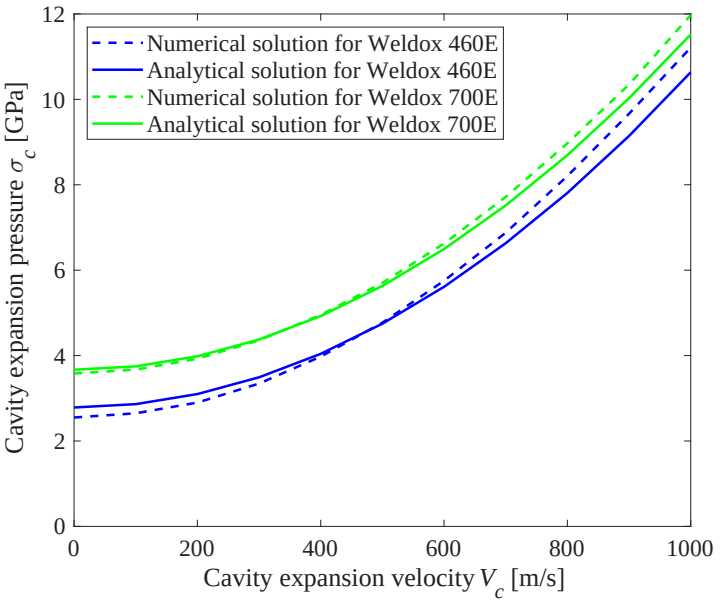

Fig. 4. Numerical and analytical solutions for cavity-expansion pressures as a function of cavity-expansion velocity for steels Weldox 460E [20] and Weldox 700E [21]. Analytical solutions are obtained using Eq. (2.44).

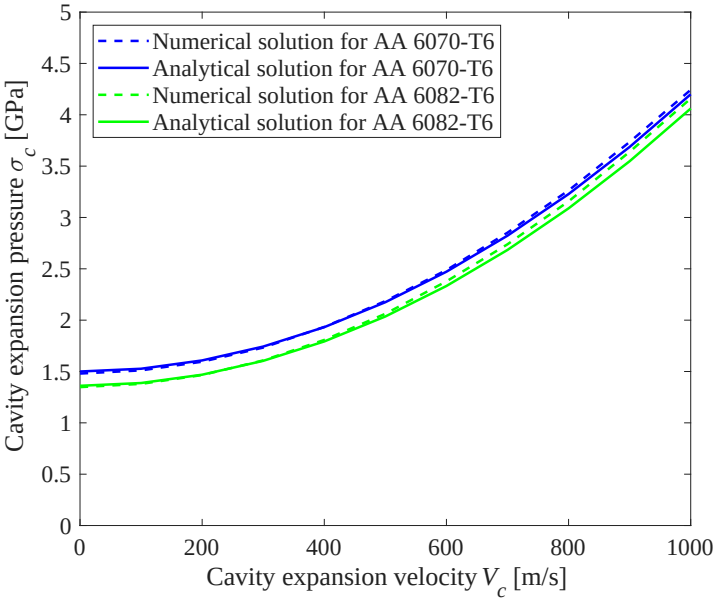

Fig. 5. Numerical and analytical solutions for cavity-expansion pressures as a function of cavity-expansion velocity for aluminium alloys AA6070-T6 [22] and AA6082-T6 [23]. Analytical solutions are obtained using Eq. (2.44).

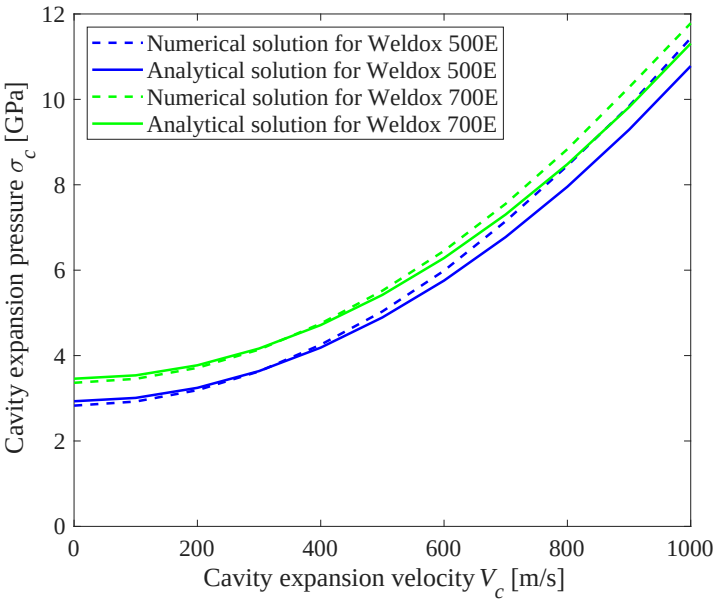

FIG. 6. Numerical and analytical solutions for cavity-expansion pressures as a function of cavity-expansion velocity for steels Weldox 500E [24] and Weldox 700E [24]. Analytical solutions are obtained using Eq. (2.44).

which were calculated by Eq. (2.44), are reported in Table 4. Besides, the coefficient of determination R_d^2 has also been calculated and serves as the criteria for the goodness of fit. High values of R_d^2 confirm the validity of the proposed polynomial approximation of the cavity-expansion pressure as well as indicate a reasonably accurate analytical solution based on by Eq. (2.44).

TABLE 4. Fitted and analytical values of coefficients A_0 and A_2 in the polynomial representation of the cavity-expansion pressure for various aluminium alloys and steels.

Materials	A_0		A_2		R_d^2	
	Fitted	Eq. (2.44)	Fitted	Eq. (2.44)	Fitted	Eq. (2.44)
AA 7075-T651 [18]	4.6446	4.9164	0.9770	1	0.9999	0.9706
AA 5083-H116 [19]	10.5736	11.5768	1.0876	1	0.9998	0.9920
Weldox 460E [20]	5.2262	5.6824	1.1171	1	1.0000	0.9888
Weldox 700E [21]	4.1940	4.2710	1.0682	1	1.0000	0.9944
AA6070-T6 [22]	4.2407	4.2854	1.0294	1	0.9999	0.9992
AA6082-T6 [23]	4.4067	4.4282	1.0449	1	1.0000	0.9969
Weldox 500E [24, 25]	5.0096	5.1610	1.1102	1	1.0000	0.9863
Weldox 700E [24, 25]	4.5674	4.6848	1.0871	1	1.0000	0.9919

4.2. Ballistic performance

To ensure comprehensive validation, the model predictions are compared to ballistic experimental data for different aluminium alloy and steel plates.

Residual velocity

Residual velocity–impact velocity relation provides a useful evaluation of ballistic performance of the target under a ballistic impact. Comparisons between analytical solutions and experimental data for the residual velocity of different penetrators under normal impact on aluminium alloy AA 7075-T651, AA 5083-H116, AA6070-T6 plates as well as steel Weldox 460E and Weldox 700E plates are illustrated in Figs. 7–12. Good agreement was observed between the model predictions and experimental data for the residual velocity.

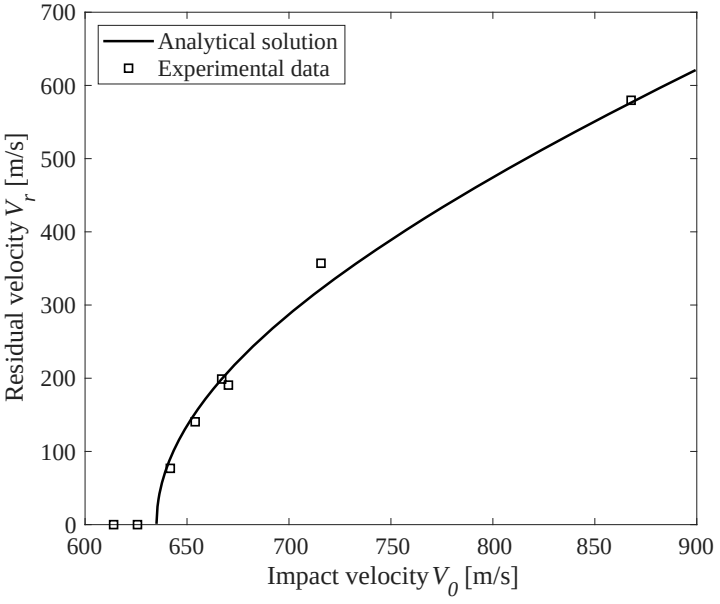

Fig. 7. Ballistic performance of 20 mm-thick AA 7075-T651 plate under normal impact of ogival-nosed penetrator ($d = 6.17$ mm, $M = 5.25$ g, CRH $= 3$). Experimental data [18].

Ballistic limit

The most common method for evaluating ballistic performance of a given target is the ballistic limit V_b, a key parameter in armor design. The ballistic limit provides a direct measure of the energy dissipation within the target material during impact. Comparisons between the analytical prediction for ballistic limit based on Eq. (3.23) and experimental data for ballistic limits of different

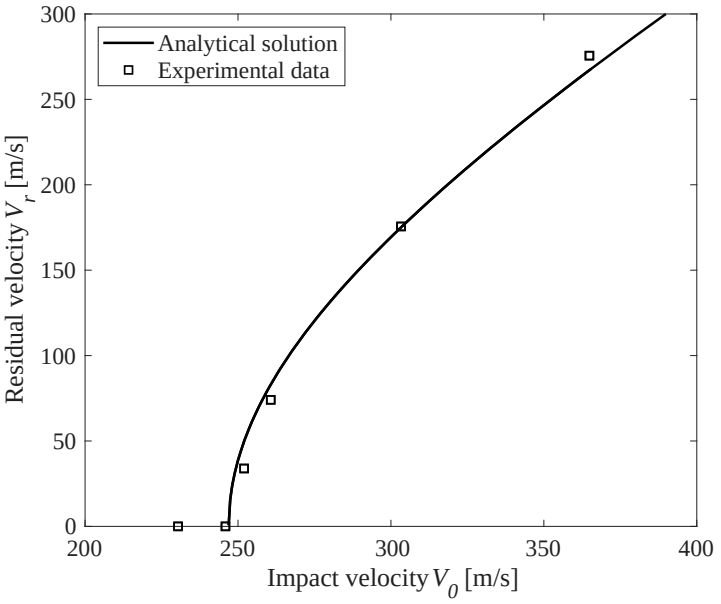

Fig. 8. Ballistic performance of 20 mm-thick AA 5083-H116 plate under normal impact of conical-nosed penetrator ($d = 20$ mm, $M = 197$ g, $\phi = 16.7^\circ$). Experimental data [19].

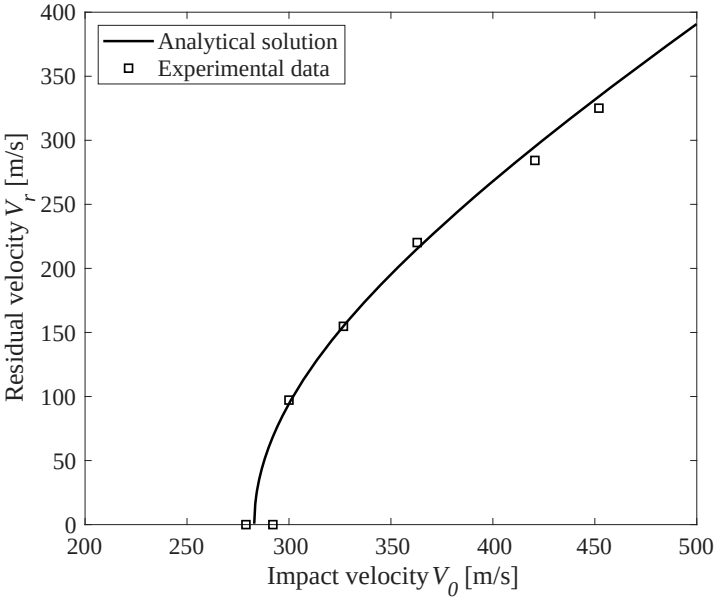

Fig. 9. Ballistic performance of 12 mm-thick Weldox 460E plate of under normal impact of hemispherical-nosed penetrator ($d = 20$ mm, $M = 197$ g). Experimental data [20].

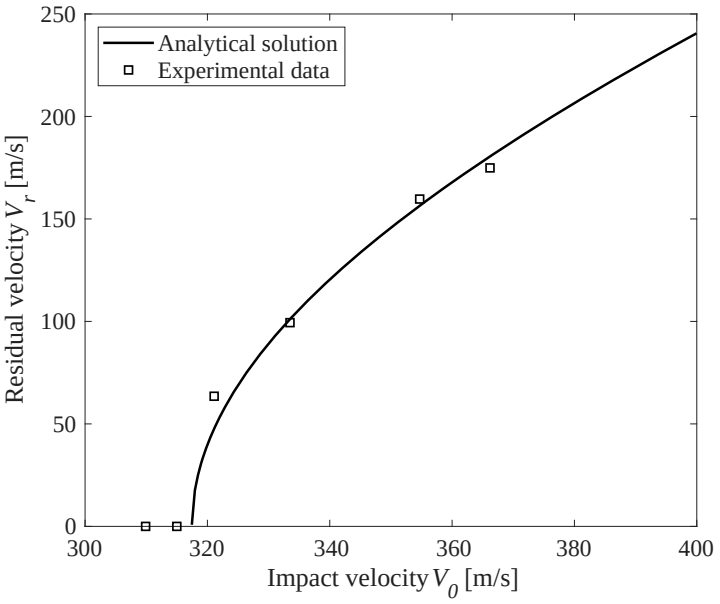

Fig. 10. Ballistic performance of 12 mm-thick Weldox 700E plate of under normal impact of ogival-nosed penetrator ($d = 20$ mm, $M = 197$ g, CRH $= 3$). Experimental data [21].

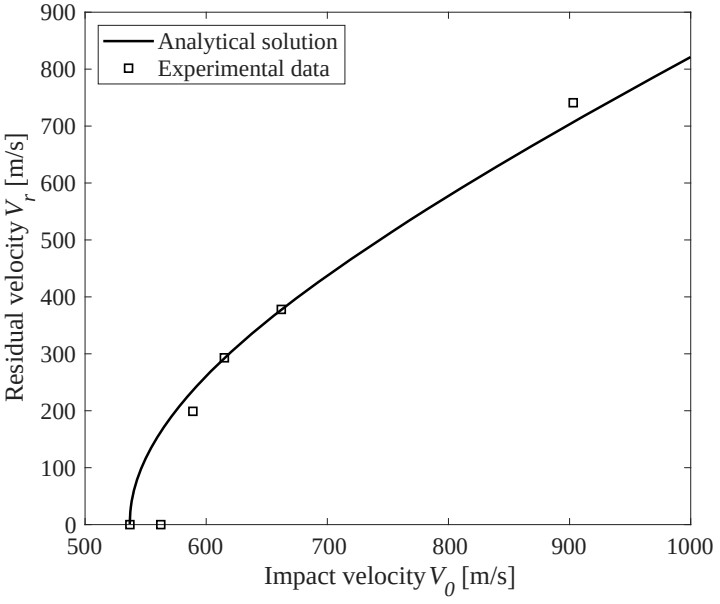

Fig. 11. Ballistic performance of 20 mm-thick AA6070-T6 plate under normal impact of ogival-nosed penetrator ($d = 6.1$ mm, $M = 5$ g, CRH $= 3$). Experimental data [22].

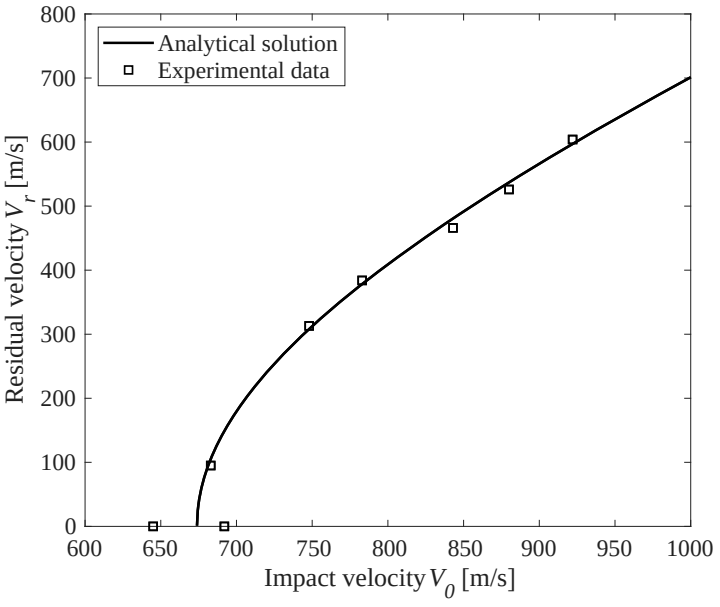

Fig. 12. Ballistic performance of 12 mm-thick Weldox 700E plate under normal impact of ogival-nosed penetrator ($d = 6.1$ mm, $M = 5$ g, CRH = 3). Experimental data [25].

aluminium alloy and steel plates are illustrated in Table 5 and demonstrate close alignment. Notably, the phenomenological scaling factor φ introduced to adjust the target resistance, was determined through a least-squares regression of Eq. (3.22) fitted to the experimental residual velocity–impact velocity data presented in the previous section.

Table 5. Comparison between analytical prediction and experimental measurement for ballistic limits of various aluminium alloy and steel plates.

Target plate		Penetrator			φ [–]	Ballistic limit V_b [m/s]	
Materials	Thickness h [mm]	Diameter d [mm]	Mass M [g]	Nose shape (O, C, H)*		Experimental measurement	Analytical Eq. (3.23)
AA 7075-T651	20	6.17	5.25	O, CRH = 3	1.28	625.7 [18]	635.0
AA 5083-H116	20	20	197	C, $\phi = 16.7°$	1.51	245.9 [19]	247.0
Weldox 460E	12	20	197	H	1.40	292.1 [20]	283.0
Weldox 700E	12	20	197	O, CRH = 3	1.41	318.1 [21]	317.5
AA 6070-T6	20	6.1	5.0	O, CRH = 3	1.25	562.5 [22]	536.3
Weldox 700E	12	6.1	5.0	O, CRH = 3	1.13	675 [25]	673.9

*Note: O – ogival, C – conical, H – hemispherical.

4.3. Discussion

The results indicate strong agreement between the predicted and observed values of residual velocities and ballistic limits, affirming the model's capability to capture the interaction between the projectile and the target during the penetration phase. Nevertheless, the use of residual velocity data for validation may introduce potential limitations, particularly due to free-surface effects that are not explicitly included in the current model. Penetration depth data, which is more representative of the material's response during the penetration process, would provide a more robust validation.

It should be emphasised that the present spherical cavity-expansion formulation assumes a semi-infinite medium and does not explicitly account for rear free-surface unloading. In finite-thickness targets, a release wave originating from the rear surface reduces the confinement in the final stage of penetration, which may slightly decrease the effective resistance during perforation. For the plate thickness-to-projectile diameter ratios considered in Figs. 7–12, the characteristic transit time of the release wave is comparable to the later phase of penetration, indicating that free-surface effects primarily influence the terminal stage rather than the entire penetration process. Based on comparisons with published experimental and numerical studies for similar configurations, the resulting deviation in predicted residual velocity is expected to be limited to several percent, typically within 5% to 10%. This magnitude is consistent with the level of agreement observed between the present model and the experimental data. Therefore, while free-surface unloading is not explicitly modelled, its influence on the reported results is considered secondary for the configurations examined.

5. Conclusion

This study developed an analytical model to predict the ballistic performance of elastoplastic materials with strain hardening under normal impact by rigid penetrators. The model incorporates the localized interaction model and the spherical cavity-expansion theory, enhanced with strain-hardening laws such as Ludwik and Voce formulations. Through a comprehensive mathematical formulation, the model successfully accounts for material behaviour, including elastic-plastic transitions and nonlinear effects such as strain hardening and high-velocity interactions.

The model's validity is confirmed through experimental data for aluminium alloys and steel plates, with excellent agreement observed between predicted residual velocities and ballistic limits and the measured results. The findings demonstrate the robustness and accuracy of the model, highlighting its potential

to serve as a reliable and computationally efficient alternative to experimental and numerical approaches.

Moreover, the physical constraints imposed on the model parameters ensure that the predicted velocity decay aligns with the principles of penetration mechanics. This feature strengthens the applicability of the model for practical engineering scenarios, including armour design and performance evaluation.

However, the free face effect, which can influence stress distribution near the exit surface during perforation, was not explicitly considered in the current model. This simplification may limit the model's accuracy under certain conditions. Although the linear EOS used in this study provides accurate predictions for the considered velocity range, it may not fully capture the nonlinear pressure-strain. Future research will focus on extending the model to incorporate these effects to enhance predictive fidelity for such scenarios. These advancements will further broaden the scope and applicability of the model for diverse impact scenarios.

Acknowledgements

The work has been supported by the Ministry of Defence of the Czech Republic "Long Term Organization Development Plan 1011" – Military autonomous and robotic assets of the Faculty of Military Technology, University of Defence, Brno (DZRO-FVT22-VAROPS) and by the Ministry of Education, Youth and Sports of the Czech Republic (Specific Research Project No: SV25-216).

Declaration of competing interests

The authors declare that they have no competing financial interests.

References

1. R. Hill, *The Mathematical Theory of Plasticity*, Oxford University Press, Oxford, 1950.
2. M.J. Forrestal, V.K. Luk, *Dynamic spherical cavity-expansion in a compressible elastic-plastic solid*, Journal of Applied Mechanics, **55**, 2, 275–279, 1988, https://doi.org/10.1115/1.3173672.
3. V.K. Luk, M.J. Forrestal, D.E. Amos, *Dynamic spherical cavity expansion of strain-hardening materials*, Journal of Applied Mechanics, **58**, 1, 1–6, 1991, https://doi.org/10.1115/1.2897150.
4. T.L. Warren, M.J. Forrestal, *Effects of strain hardening and strain-rate sensitivity on the penetration of aluminum targets with spherical-nosed rods*, International Journal of Solids and Structures, **35**, 28–29, 3737–3753, 1998, https://doi.org/10.1016/S0020-7683(97)00211-4.

5. Q. Fang, X. Kong, J. Hong, H. Wu, *Prediction of projectile penetration and perforation by finite cavity expansion method with the free-surface effect*, Acta Mechanica Solida Sinica, **27**, 6, 597–611, 2014, https://doi.org/10.1016/S0894-9166(15)60005-2.

6. I. Ga, D. Noh, J.W. Yoon, *Spherical cavity expansion method dependent on strain, strain rate, and temperature*, International Journal of Impact Engineering, **181**, 104730, 2023, https://doi.org/10.1016/j.ijimpeng.2023.104730.

7. M.J. Forrestal, T.L. Warren, *Penetration equations for ogive-nose rods into aluminum targets*, International Journal of Impact Engineering, **35**, 8, 727–730, 2008, https://doi.org/ 10.1016/j.ijimpeng.2007.11.002.

8. T.L. Liu, X.F. Wang, B. Jia, Y.X. Xu, *Oblique penetration of tungsten spheres against steel targets based on compressible and incompressible cavity expansion theory*, International Journal of Impact Engineering, **188**, 104914, 2024, https://doi.org/10.1016/j.ijimpeng.2024.104914.

9. Z. Rosenberg, E. Dekel, *Analytical solution of the spherical cavity expansion process*, International Journal of Impact Engineering, **36**, 2, 193–198, 2009, https://doi.org/10.1016/j.ijimpeng.2007.12.014.

10. D. Durban, R. Masri, *Dynamic spherical cavity expansion in a pressure sensitive elastoplastic medium*, International Journal of Solids and Structures, **41**, 20, 5697–5716, 2004, https://doi.org/10.1016/j.ijsolstr.2004.03.009.

11. T. He, H.-M. Wen, X.-J. Guo, *A spherical cavity expansion model for penetration of ogival-nosed projectiles into concrete targets with shear-dilatancy*, Acta Mechanica Sinica, **27**, 6, 1001–1012, 2011, https://doi.org/10.1007/s10409-011-0505-1.

12. Y.J. Deng, X.W. Chen, W.J. Song, *Dynamic cavity-expansion penetration model of elastic-cracked-crushed response for reinforced-concrete targets*, International Journal of Impact Engineering, **157**, 103981, 2021, https://doi.org/10.1016/j.ijimpeng.2021.103981.

13. M. Alaei Varnosfaderani, P. Maghoul, N. Wu, *Modelling the penetration of subsonic rigid projectile probes into granular materials using the cavity expansion theory*, Computers and Geotechnics, **141**, 104546, 2022, https://doi.org/10.1016/j.compgeo.2021.104546.

14. J.D. Walker, *Modern Impact and Penetration Mechanics*, Cambridge University Press, Cambridge, 2021.

15. G. Ben-Dor, A. Dubinsky, T. Elperin, *Ballistic impact: Recent advances in analytical modeling of plate penetration dynamics – A review*, Applied Mechanics Reviews, **58**, 6, 355–371, 2005, https://doi.org/10.1115/1.2048626.

16. B.T. Phan, R. Vítek, J. Viliš, V. Horák, *An analytical model for ballistic performance of fiber-reinforced plastic laminates*, Applied Composite Materials, **32**, 4, 1639–1657, 2025, https://doi.org/10.1007/s10443-025-10344-2.

17. X.W. Chen, Q.M. Li, *Deep penetration of a non-deformable projectile with different geometrical characteristics*, International Journal of Impact Engineering, **27**, 6, 619–637, 2002, https://doi.org/10.1016/S0734-743X(02)00005-2.

18. K. Senthil, M.A. Iqbal, P.S. Chandel, N.K. Gupta, *Study of the constitutive behavior of 7075-T651 aluminum alloy*, International Journal of Impact Engineering, **108**, 171–190, 2017, https://doi.org/10.1016/j.ijimpeng.2017.05.002.

19. T. Børvik, M.J. Forrestal, O.S. Hopperstad, T.L. Warren, M. Langseth, *Perforation of AA5083-H116 aluminium plates with conical-nose steel projectiles – Calculations*, International Journal of Impact Engineering, **36**, 3, 426–437, 2009, https://doi.org/10.1016/j.ijimpeng.2008.02.004.

20. T. Børvik, M. Langseth, O.S. Hopperstad, K.A. Malo, *Perforation of 12 mm thick steel plates by 20 mm diameter projectiles with flat, hemispherical and conical noses: Part I: Experimental study*, International Journal of Impact Engineering, **27**, 1, 19–35, 2002, https://doi.org/10.101/S0734-743X(01)00034-3.

21. S. Dey, T. Børvik, X. Teng, T. Wierzbicki, O.S. Hopperstad, *On the ballistic resistance of double-layered steel plates: An experimental and numerical investigation*, International Journal of Solids and Structures, **44**, 20, 6701–6723, 2007, https://doi.org/10.1016/j.ijsolstr.2007.03.005.

22. J.K. Holmen, J. Johnsen, S. Jupp, O.S. Hopperstad, T. Børvik, *Effects of heat treatment on the ballistic properties of AA6070 aluminium alloy*, International Journal of Impact Engineering, **57**, 1, 119–133, 2013, https://doi.org/10.1016/j.ijimpeng.2013.02.002.

23. J.K. Holmen, T. Børvik, O.R. Myhr, H.G. Fjær, O.S. Hopperstad, *Perforation of welded aluminum components: Microstructure-based modeling and experimental validation*, International Journal of Impact Engineering, **84**, 1, 96–107, 2015, https://doi.org/10.1016/j.ijimpeng.2015.05.016.

24. J. Johnsen, J.K. Holmen, T.L. Warren, T. Børvik, *Cylindrical cavity expansion approximations using different constitutive models for the target material*, International Journal of Protective Structures, **9**, 2, 199–225, 2018, https://doi.org/10.1177/2041419617741321.

25. T. Børvik, S. Dey, A.H. Clausen, *Perforation resistance of five different high-strength steel plates subjected to small-arms projectiles*, International Journal of Impact Engineering, **36**, 7, 948–964, 2009, https://doi.org/10.1016/j.ijimpeng.2008.12.003.

Received October 21, 2025; revised version March 11, 2026.
Published online April 28, 2026.